Impact of a thin inhomogeneous snow layer on a microwave corner reflector RADAR cross section: consequences for spaceborne remote sensing

Jean-Michel Friedt

Abstract—The dramatic reduction in microwave RADAR corner reflector backscattered power when coated with even a thin layer of snow is investigated and the impact on spaceborne RADAR remote sensing in polar regions is assessed. Time series over two years of Sentinel-1 measurements in Spitsbergen (Arctic Norway, 79°N) are interpreted in view of this analysis. The refraction of the incoming microwave beam preventing the backscattered signal from reaching the monostatic RADAR is reproduced in laboratory controlled experiments demonstrating that low-loss dielectric layers not parallel to the corner reflector conducting sides are the cause of the signal loss.

Index Terms—Corner reflector, spaceborne RADAR, snow, polar regions

I. INTRODUCTION

WITH the advent of numerous spaceborne RADARs, including the Chinese Gaofen-3, German Terra-SAR, Canadian RADARSAT (-2 and Constellation Mission currently active), Japanese ALOS2, European Sentinel-1, commercial service by Umbra and the forthcoming American/Indian NISAR, using radiofrequency signals for remote sensing has become a popular approach [1]–[7] thanks to its insensitivity to cloud cover or illumination conditions, allowing for all-weather remote sensing. This statement is especially true in polar regions with its dense cloud cover during summer and polar night during winter hindering optical remote sensing, even more with the continuously mapping and freely available ESA data and the future NISAR claiming open data policy [8] and continuous extensive mapping [9]. These remote sensing platforms meet the need for continuous global snow cover extent mapping [10].

Beyond using reflectivity maps or phase analysis for fine displacement detection (InSAR) on persistent scatterers of opportunities, numerous authors have considered using corner reflectors as cooperative targets for remote sensing measurements in the cryosphere [11]–[13] in the continuity of the original insight leading to RadioFrequency IDentification [14] (RFID), paving the path towards modulating the backscattered signal with environmental parameters. Indeed, snow covering a corner reflector will impact polarization rotations and phase shift, allowing to recover snow properties through remote sensing measurements using passive cooperative targets [15]. Although the electric field reflected by corner reflectors has

been simulated for a long time [16]–[18] using techniques involving geometrical and physical optics, the case of a thin dielectric layer coating one or multiple sides of the corner reflector in a layer not parallel to the conductor has not been addressed analytically: this paper aims at developing some field observations and interpreting experimental laboratory results of such measurement conditions experimentally and will not be concerned with modelling beyond a basic two-dimensional (2D) raytracing intuitive insight into the cause of the backscattered signal loss. Corner reflectors are made of three planar conducting surfaces mounted at right angle so that the incoming electromagnetic field is backscattered towards the same direction as the incident beam: they act as strong reflectors with little dependence on azimuth-elevation orientation with respect to the monostatic RADAR incoming beam. Their wide use is due to the small, point-like target when considering spaceborne illumination RADAR sources, with respect to the background clutter backscattered by all surfaces lying in each illuminated pixel. Analytical RADAR cross section expressions exist for the trihedral triangular and square corner reflectors where each surface assembled at right angle are respectively an isosceles right triangle with short side length a or square with side length a, as will be used later in this section. The RADAR cross section (RCS) σ is defined in the RADAR equation relating the backscattered power P_R per unit solid angle (W) to the incident power density P_I (W/m^2) ratio as

$$\frac{P_R}{P_I} = \frac{1}{4\pi}\sigma$$

with unit m^2: σ thus represents the effective area intercepting the incoming RADAR power and scattering back isotropically to the RADAR receiver. Since the RCS appears at the numerator of the RADAR link budget, with the denominator including the fourth power of the distance in a monostatic configuration and the numerator the receiving antenna effective area (or the wavelength squared times the antenna gain), any drop in RCS leads to a drop in detection range or in signal to noise ratio on the received signal.

Three corner reflectors are deployed in the Ny-Ålesund area in Spitsbergen (Arctic Norway, 79°N): a historical large reflector located near the airstrip was installed by Dan J. Weydahl (FFI) at 78.92001°N, 11.88322°E in the 1990s for monitoring ERS signals [19]. From September 2021 to May 2024, a 96-cm trihedral triangular corner reflector has been installed by the author next to Corbel station, 5 km East of Ny-Ålesund,

at ground level in a setup relevant to the installation of such a

cooperative target for glacier melt and flow remote sensing or landslide displacement measurement, e.g. on the nearby Austre Lovén glacier. Finally, since September 2023, a 0.75 cm trihedral square corner reflector was installed by a Polish team in the context of the CRIOS grant (https://crios.pl/), 200 m West of Corbel station, elevated by a couple of meters over the ground. All the corner reflectors considered in this study are facing westward.
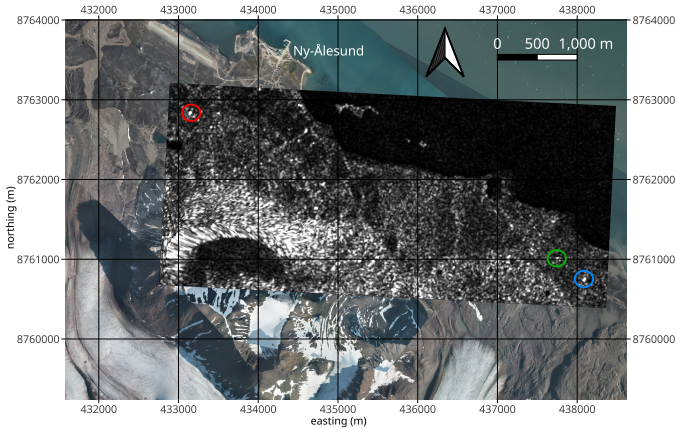

Fig. 1. Geographical setting: the background picture (orthophoto from the Norwegian Polar Institute available from https://geodata.npolar.no/) displays the Ny-Ålesund area where three corner reflectors are located. The historical corner reflector setup by the Norwegian FFI in red, the latest Polish corner reflector in green, and our setup next to Corbel station in blue. The grid refers to WGS84/UTM33N coordinates. The overlaid Sentinel-1 backscattered coefficient map was fetched from https://apps.sentinel-hub.com/eo-browser as the linear scale gamma0 backscattered coefficient with radiometric and terrain corrections: this particular map was collected September 11, 2023.

All corner reflectors are well visible on the Sentinel-1 backscattered signal maps (Fig. 1) when snow is absent, and the expectation was for the second (Corbel) corner reflector (Fig. 2) to remain visible during the polar night since the dry, cold snow is well known to be transparent to electromagnetic waves, as assessed commonly when using Ground Penetrating RADAR for sub-surface glacier bedrock or snow layering mapping [20]. However, it was observed that even a shallow snow cover significantly decreases the backscattered signal power detected by the spaceborne RADAR, while the signal was recovered if either snow was manually removed from the corner reflector or melt occurred. This observation matches the conclusion of other researchers deploying corner reflectors in snow-covered areas who made sure to prevent snow from reaching the corner reflector surfaces [21] or cleaned the surfaces from accumulated snow prior to satellite observations.

The objective of this work is to understand the cause of the backscattered signal loss despite the low microwave absorbance of the cold (sub-0°C) snow and relate the reflected power with snow cover conditions. We focus on the trihedral triangular corner reflector we deployed at ground level near Corbel station, with a 96-cm side and facing Eastward at an elevation of 20° tuned for Sentinel-1 descending morning passes (6h15–06h17 UTC).
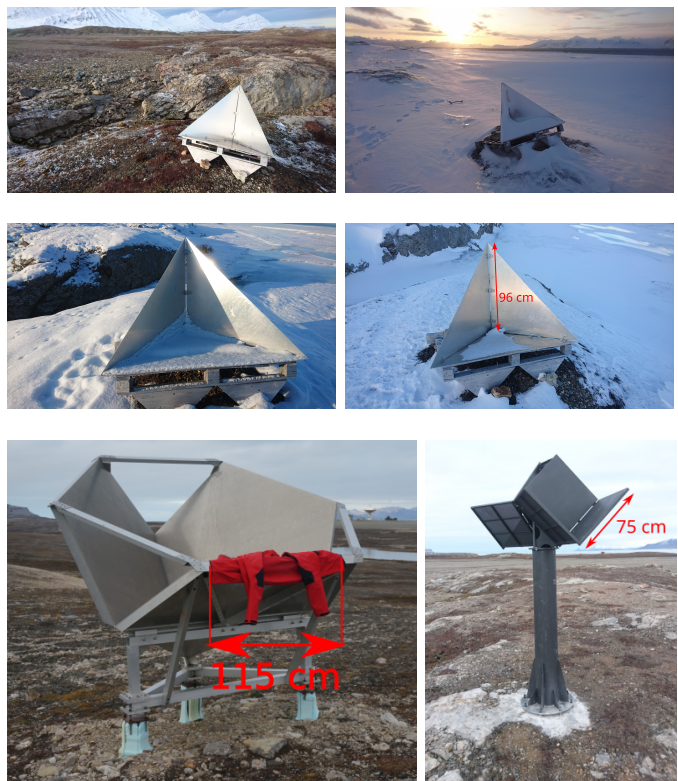

Fig. 2. Top: bare COR corner reflector pictured September 13, 2022, and the same corner reflector filled with snow pictured on April 21, 2023. Middle: COR corner reflector picture taken Sept. 23, 2023 with a snow cover sufficient to reduce backscattering by 17.9 dB with respect to the clean corner reflector, and Oct. 05, 2023 with minute backscattering loss of 0.2 dB with respect to the clean corner reflector. Bottom: the NYA reference corner reflector (left) and the POL reference corner reflector (right).

II. FIELD MEASUREMENTS

Beyond the few pictures shown for illustration purposes in Fig. 2 under various snow cover conditions, continuous backscattered signal measurements were performed on Sentinel-1 datasets available from the ESA Copernicus web site at apps.sentinel-hub.com/eo-browser (Fig. 3, top).

The Corbel corner reflector was installed in September 2021, prior to the failure of Sentinel-1B on December 23rd, 2021, so that the initial time interval between measurements is 6 days. After December 24th, 2021, with only Sentinel-1A remaining, the measurement period rises to 12 days. The reflected magnitude is measured as the maximum value of a 30×30 pixel region of interest centered on each corner reflector location clearly visible in a snow-free acquisition (Fig. 1, bottom). The *floating point* GeoTIFF files were used for this analysis since the integer (8 or 16-bit) GeoTIFF files provided by ESA are saturated when the corner reflectors are snow free. However, most TIFF file reading packages are unable to handle floating point values (e.g. GNU Octave): all analysis were performed with files read using the OpenCV2 library of Python3. For comparison, the backscattered magnitude from two reference areas (REF1 and REF2) are also displayed where no corner reflector is installed to display the seasonal variation in the absence of a cooperative target. The
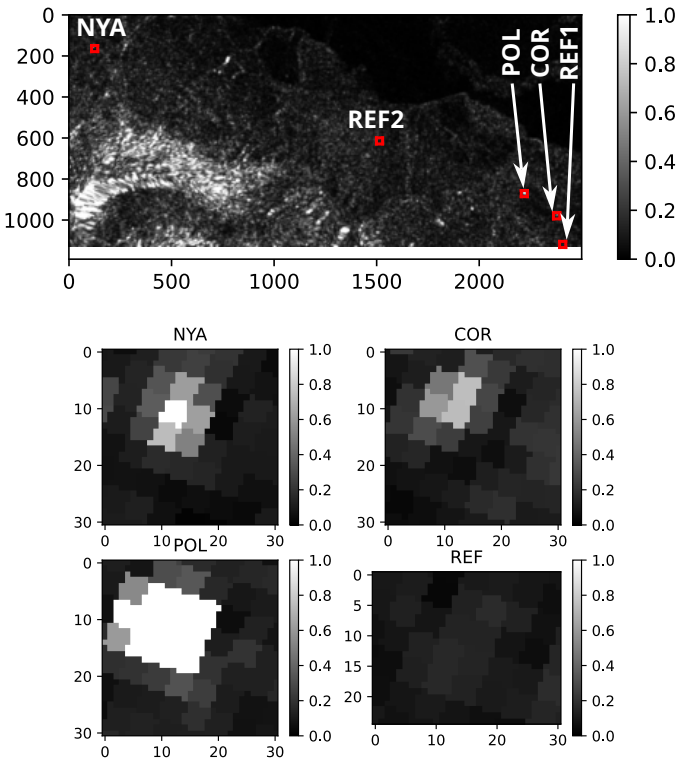
Fig. 3. GeoTIFF file with floating point value map of the reflected power (top) with the location of the regions of interest, and zoom on each region of interest centered on the corner reflectors located in the surveyed area. REF refers either to REF1 or REF2 since in both cases, background reflected power is assessed to measure the limit of detection in areas where no artificial reflector is located. X and Y axis are all graduated in arbitrary unit pixel index.

24 h as recorded on the Seklima Norwegian weather database is displayed on Fig. 4 (bottom). Some discrepancy might be observed during 2022 when the corner reflector was manually freed from snow during maintenance session by the wintering staff as indicated by green vertical dashes and dates above the second chart. The precipitations – solid for filling the corner reflector or liquid removing the accumulated snow – only provides a partial information justifying the loss of backscattered signal since wind blown transport is significant for the low-elevation COR corner reflector.
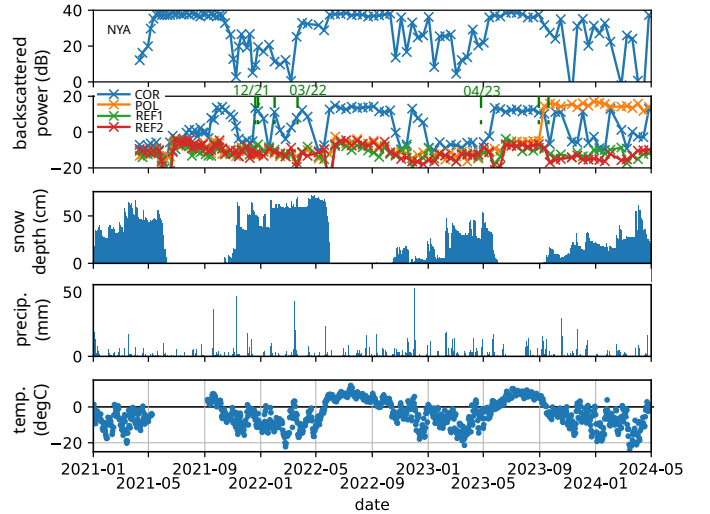

Fig. 4. Two charts from top: reflected power measured by Sentinel-1 of the NYA reference corner reflector (top) and the Corbel station (COR), Polish (POL) and background reference patches (REF1 and REF2). The results were spread on two separate charts due to the widely varying Y-axis ranges since the NYA reflector RADAR Cross Section is much larger than the smaller COR and POL corner reflectors. The vertical green lines on the second chart from top indicate the dates when the COR corner reflector was cleaned free of snow in December 20 and 26, 2021 and in January 31, 2022. The corner reflector was also manually cleaned from snow March 22, 2022, April 26, 2023 and Sept. 20, 2024. POL was installed end of Aug. 2024. Third from top: snow depth measured at Ny-Ålesund station according to the seklima.met.no database (SN99910). Fourth from top: precipitations at Ny-Ålesund station according to the seklima.met.no database. Bottom: 24-h mean air temperature from the seklima.met.no database in Ny-Ålesund.

installation of the Corbel (COR) and Polish (POL) corner reflectors is clearly visible as a rise of the backscattered signal. Prior to the installation of each one of these corner reflectors, the backscattered signal is representative of the seasonal variation of the background signal, as are REF1 and REF2. The FFI corner reflector in Ny-Ålesund (NYA) exhibits a strong backscattered signal and is displayed on a different chart with appropriate scales. The COR and POL corner reflectors are simple geometries whose RCS can be estimated: COR is a $a = 96$ cm long triangular trihedral corner reflector expected to exhibit $RCS = \frac{4\pi a^4}{3\lambda^2}$ at $\lambda = 5.55$ cm for the 5.405 GHz signal emitted by Sentinel-1, and POL is a $a = 0.75$ m long square trihedral corner reflector expected to exhibit $RCS = \frac{12\pi a^4}{\lambda^2}$. The numerical values lead to respectively 1155 m^2 and 3870 m^2 or a ratio of 3.3 on the returned power, leading to a returned amplitude ratio of $\sqrt{3.3} \simeq 1.8$, close to the observed ratio is about 1.5 in a linear scale, or in logarithmic scale to $10 \cdot \log_{10}(3.3) \simeq 5.2$ dB. The NYA corner reflector is a complex shape whose RCS cannot be estimated analytically (Fig. 2, bottom left).

The drop in signal from the Corbel corner reflector (Fig. 4, second from top, blue curve), is correlated with the snow depth (Fig. 4, third chart from top), with a maximum backscattered signal in Summer and Autumn but a sharp drop as soon as the first snow fall occurs. For comparison, the Ny-Ålesund precipitations, snow depth and air temperature averaged over

An Onset Hobo temperature logger was set on the corner reflector in April 2023, with the shielded internal temperature probe measuring the air temperature in a shadow environment and the external probe closely bonded to the surface exposed to the sky of the bottom plate of the corner reflector. The objective was to assess snow cover through the insulating impact of snow to air temperature variations: when both temperature probe measurements differ most, snow is considered to cover the external sensor and shield it from environmental temperature variations.

On the other hand when snow has melted, the probe exposed to direct sunlight heats due to convection and radiation and exhibits wider temperature variations than the shadowed sensor. Indeed on Fig. 5, a red rectangle on the bottom chart highlights the significant temperature difference between both sensors at the melt season between May 14, 2023 and May 26, 2023, the two dates of Sentinel-1A measurements. While the external probe (orange) is covered with snow, its temperature variations
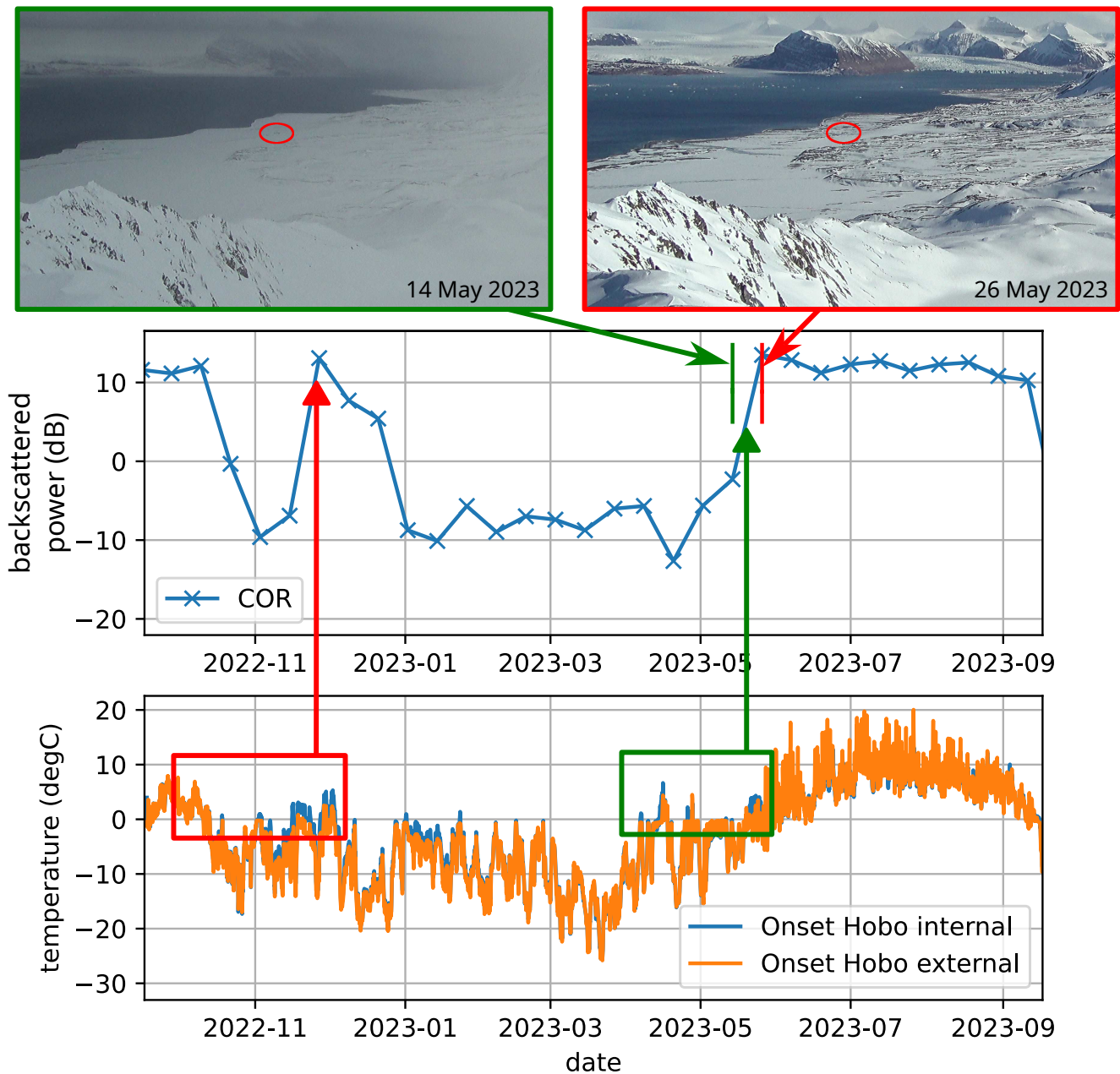
Fig. 5. Top: COR corner reflector backscattered power (dB as $20 \cdot \log_{10}()$ of the amplitude signal recorded by Sentinel-1 in the Interferometric Wide maps) during 2023 season from April 25, 2023 to September 20, 2023. Middle: zoom on the region of interest of the Zeppelin station webcam facing Eastward toward the Corbel corner reflector whose approximate location at sea level elevation is indicated by the red ellipses. Bottom: temperature at the corner reflector location, in blue air temperature under shadow conditions (internal probe) and in orange the external probe bonded using heat conducting tape to the bottom side of the corner reflector facing the sky. The red rectangle indicates when the two temperature probe measurements differ, indicating the external probe temperature fluctuations are damped by the insulation of the snow cover remaining on the corner reflector. Overlapping blue and orange curves indicate consistent measurements by both probes exposed to air. Once the snow has melted, the external probe exhibits sharp temperature rises when heated by direct sunlight.

are smaller than the one measuring the air temperature (blue) due to the thermal insulation of snow and cannot rise above 0°C (red and green rectangles on the bottom chart of Fig. 5). On the other hand once snow has melted, the external probe exposed to direct sunlight warms up faster than the shadowed internal probe, as seen from June to September.

The sharp rise in backscattered signal power (Fig. 5, top chart) by 20 dB matches the snow melt detected from the temperature difference between both probes, and matches the visual snow cover seen on the Zeppelin station (www.npolar.no/en/zeppelin/) webcam collected from data.npolar.no/_file/zeppelin/camera/Panorama/2023-05 when selecting the 12:01 UTC picture facing Eastward. Uniform snow cover is visible on the May 14, 2023 picture (green) and the May 13th 12:01 UTC picture is not displayed since it exhibits a uniformly
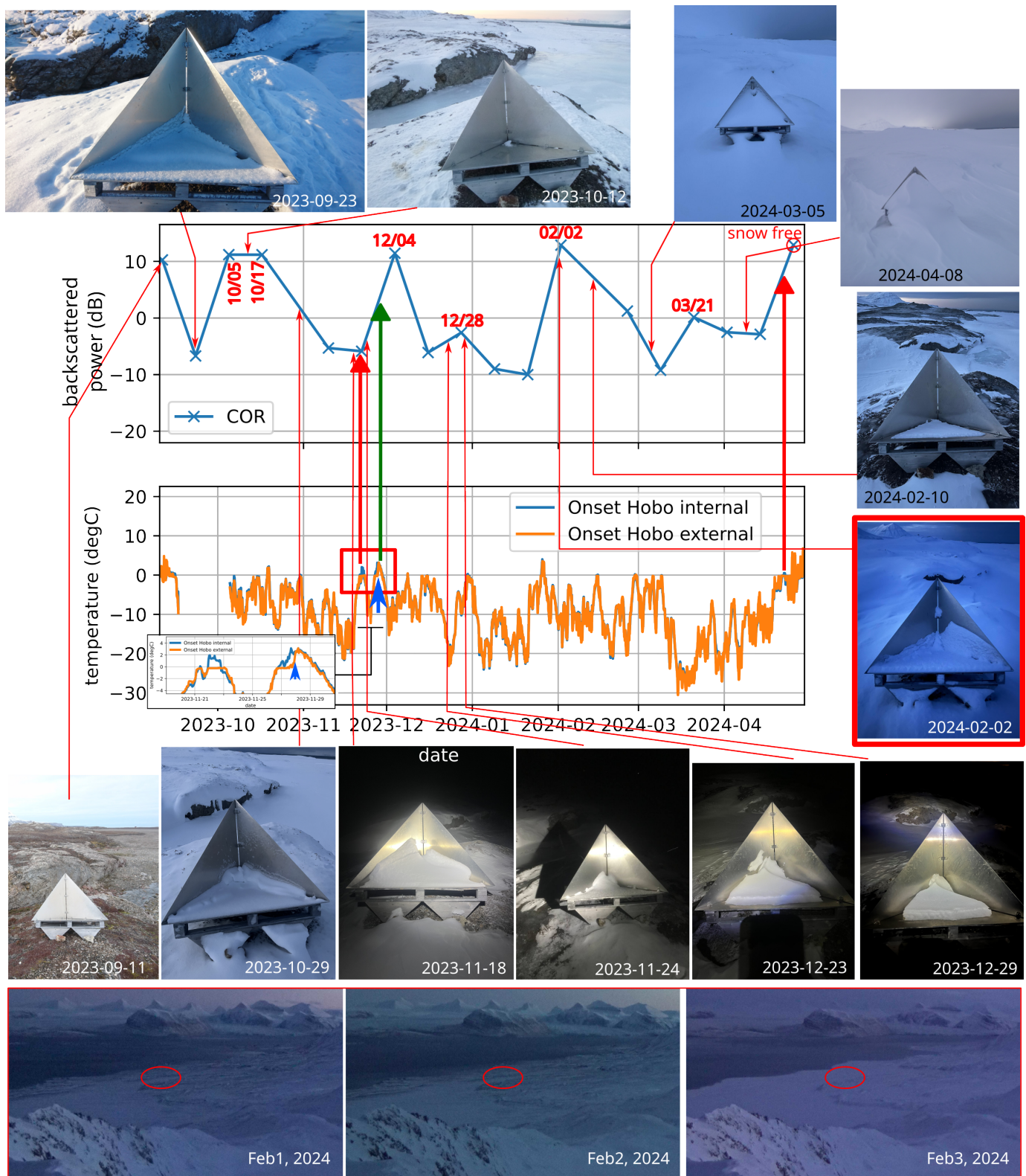
Fig. 6. Zoom on the winter 2023-2024 season: top the reflected RADAR power recorded by Sentinel-1 on the COR, POL and REF locations, related to the actual corner reflector snow cover as recorded with pictures by wintering IPEV staff A. Pibarot. Bottom: a temperature logger was located next to the corner reflector with the internal temperature probe recording air temperature and the external temperature probe glued using thermally conducting adhesive to the corner reflector bottom surface. A large difference between the two probe measurements hints at a snow layer covering the external probe damping the air temperature variations by acting as an insulator, while overlapping blue and orange curves indicate consistent measurements by both probes exposed to air. Snow melt is detected as the external probe rising above 0°C highlighted with the blue arrow on the main chart and the inset, matching the sudden rise in the backscattered power (green arrow). Bottom: Zeppelin station webcam pictures facing the general direction where the COR corner reflector is located (red ellipse) acquired Feb 1, 2 and 3 2024 at noon, hinting at increased snow cover between Feb 2 and 3 most easily seen on the foreground ridge but also at the background sea level atltitude.

white image attributed to heavy snow fall, whereas patches of snow-melt and river runoffs in dark blue are visible in the May 26, 2023 picture (red). The red ellipse on both images roughly indicate the area where the COR corner reflector is located at sea level elevation.

A similar analysis is performed on the winter-spring 2023 period (Fig. 6) with a detailed comparison with pictures of the corner reflector. Again the analysis matches the relation between inhomogeneous dry snow layer covering at least one side of the corner reflector leading to backscattered power loss. When pictures are not available, the external temperature probe fitted to the bottom side of the corner reflector comparison with the shielded air temperature probe allows for assessing snow filling the corner reflector: as highlighted (red rectangle in the bottom chart of Fig. 6 magnified in the inset to the bottom-left) the external probe temperature is limited to a maximum of $0°C$ when covered with snow while the internal air temperature probe rises above this value. The snow melt detected as the external probe rising above $0°C$ (blue sharp arrow on the main chart and the inset) around December 4, 2023 matches the sudden rise in the backscattered power (green arrow). The only mismatch in this analysis is February 2, 2024, when the picture acquired after noon (highlighted with a red border) displays a thick snow layer in the corner reflector while the backscattered signal recorded early in the morning is strong. The Zeppelin webcam picture (bottom, acquired at noon every day indicated on the bottom-right of each picture) does display an evolution from weak snow cover to heavy snow cover in the moraine area surrounding the corner reflector location (red ellipse) between Feb 2 and 3, but the impact on the corner reflector is not conclusive from such a long range observation.

III. LABORATORY MEASUREMENTS

In order to demonstrate the impact of a dielectric layer with negligible microwave absorption but with various geometries on the corner reflector backscattered power, the following experimental setup was assembled (Fig. 7):

- a 6–12 GHz horn antenna (A-Info Inc. LB-OH-112-20-C-SF) is connected to a vector network analyzer (Agilent N5230A) acting as a Frequency Stepped Continuous Wave (FSCW) RADAR, monitoring the reflection coefficient when emitting -10 dBm with an intermediate bandwidth of 50 kHz and collecting 2001 samples over the 6–12 GHz band.
- a 30 cm square trihedral square corner reflector is located 12.5 m from the horn antenna, well into the far field region considering the $D = 17.2$ cm aperture of the horn antenna so that the far field is reached at $2\frac{D^2}{\lambda} \simeq 1$ m. The corner reflector is tilted at an elevation of $30°$ from horizontal and facing the horn antenna in the azimuth direction,
- various dielectric layers are deposited on the corner reflector surfaces, with a backscattered coefficient recorded before and after each manipulation with the bare corner reflector to make sure the baseline remains stable.

The laboratory experimental setup differs with field measurements in two ways. First, a different frequency range
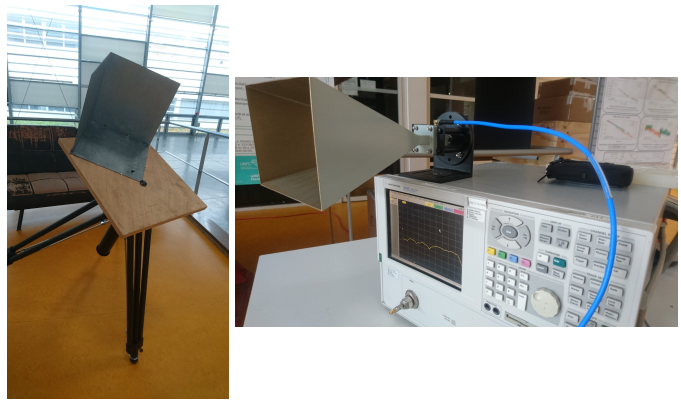

Fig. 7. Left: the corner reflector fitted to a tripod is tilted at an angle of $30°$ to the horizontal and facing the horn antenna fitted to a microwave vector network analyzer measuring the reflection scattering parameter S_{11} (right). The horn antenna to corner reflector distance is 12.5 m as ranged by the frequency-stepped RADAR analysis of the recorded S_{11}, well into the far field region.

(9000±3000 MHz instead of 5405±50 MHz for Sentinel-1) was used. This experimental setting was selected to meet the shorter distance between the monostatic antenna and the corner reflector in the laboratory setting, since the increased bandwidth improves the range resolution and the higher carrier frequency reduces the far field range. Secondly, the corner reflector shape was replaced with a square trihedral corner reflector in the laboratory to improve signal by increasing the RCS over the triangular trihedral corner reflector with similar dimensions. The resulting laboratory corner reflector RCS (275 m^2) is one fifth of that deployed in the field (1360 m^2), but the controlled environment and the lower background clutter resulting from better time-domain separation of the target leads to excellent signal to noise ratio (Fig. 8). The corner reflector backscattered power is observed to be 20 dB stronger than the tripod and surrounding holding setup.

The S_{11} reflection scattering parameters are recorded at each frequency spanning the 6000 to 12000 MHz range with 2001 steps (3 MHz steps), and post-processed (Fig. 8, top) to return to the time domain: after inverse Fourier transform to convert the frequency sweep to a time domain sweep, the time-step is $1/B = 1/6$ ns and the two-way spatial range resolution is $c/(2B) = 2.5$ cm since $B = 6$ GHz with the speed of light $c = 300$ m/μs in free space. By recording the scattering parameter with 2001 samples, a range ambiguity of 2.5 cm$\times$2001 = 50 m, allowing to clearly identify the 12.5 m range to the corner reflector. All frequency domain scattering coefficients are collected from the calibrated network analyzer and post-processed for extracting the time-domain information.

The first measurement is performed with Poly(Methyl MethAcrylate) PMMA (Fig. 8), a polymer known for its reproducible and low dielectric dissipation in the microwave band. PMMA is characterized with a relative permittivity of $\varepsilon_r = 2.6$ in the microwave region [22], [23]. The backscattered signal from a bare corner reflector is first recorded and used as baseline. A flat, 20 mm thick flat PMMA slab covering one side of the corner reflector leads to a 3 dB signal drop attributed to the impact of the vertical sides of the polymer scattering a fraction of the incoming electromagnetic energy.
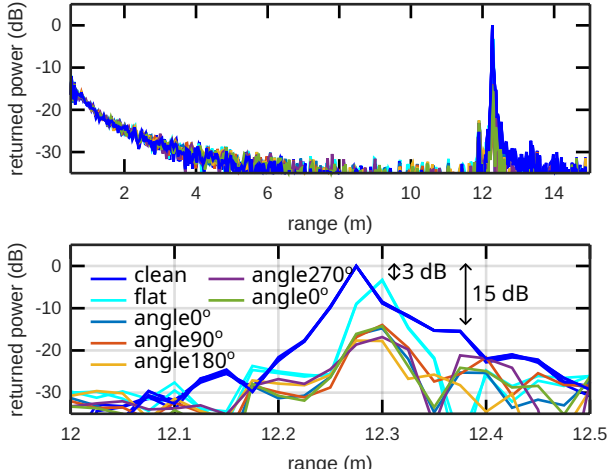
Fig. 8. Top: time-domain response after inverse Fourier transform of the frequency-domain characterization of the backscattered signal in the 6 to 12 GHz range. Bottom: reflected power for the bare corner reflector ("clean") and impact of Poly(Methyl MethAcrylate) (PMMA) parts on the bottom side of the corner reflector. First a flat 20 mm thick, 25 cm×25 cm PMMA slab is located on the bottom side of the corner reflector ("flat") leading to a 3 dB backscatter drop. The same PMMA part is machined so the thickness varies continuously from 20 mm on one side to 3 mm on the other side or an angle of 3.8°. The wedge is rotated by 90° steps on the bottom side of the corner reflector, always inducing the same 15 dB backscattered signal drop irrelevant of its orientation.
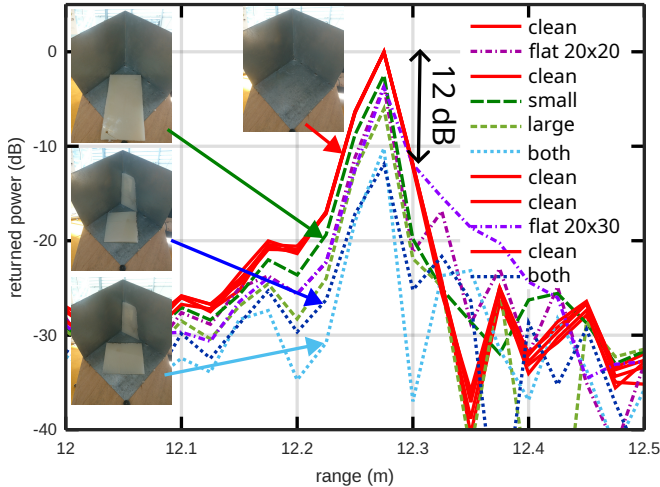

Fig. 9. Impact of PolyPropylene (PP): the 20 cm wide×17.5 cm long rectangular piece was cut from a 20 mm thick substrate to reach 0 mm on a 13 cm length or an angle of 8.7°. All overlapping red curves were collected with the bare corner reflector between each measurement with a new dielectric setting, making sure the corner reflector baseline remained stable and the setup was not moved between each measurement.

Most dramatic though is the impact of machining one of the flat sides of the PMMA so that a slope continuously ranging from 20 mm on one side to 3 mm on the other side – resulting in a wedge angle of 3.8° with the flat side facing the corner reflector face – leads to an additional 12 dB signal drop despite less material interacting with the wave. The impact of refraction is confirmed since the signal loss cannot be attributed to additional absorption by the polymer.

The experiment is repeated with PolyPropylene PP as shown

in Fig. 9 with comparable results. PP is characterized with a relative permittivity of $\varepsilon_r = 2.2$ in the microwave region [24]. In all cases the bare corner reflector signal has been recorded to make sure no part was moved when installing the polymer parts on the corner reflector side.

IV. 2D GEOMETRIC REFRACTION ANALSYSIS

Refraction of the incoming electromagnetic wave by the non-planar snow coating acts as an imperfection in the corner reflector setting, whether non-orthogonal plates in case of non-parallel flat dielectric surfaces (wedge) coating one of the reflecting surfaces, or surface inhomogeneities in the case of non-flat dielectric interfaces. The impact of such defects on the RADAR cross section has been investigated and reported in [25], [26]: 10 dB loss only requires 5 mm surface deviation on a C-band RADAR or, after correcting their erroneous equation for angle mismatch to orthogonality following [27], an angular error to orthogonality of 1.5° (Fig. 10). A flat dielectric slab coating a flat side of the conducting corner reflector at an angle acts similar to an orthogonality error due to refraction of the incoming plane wave, while a non-flat dielectric wedge coating a flat conducting side of the corner reflector impacts the backscattered power similarly to a surface deviation from the flat shape of the conducting surface.
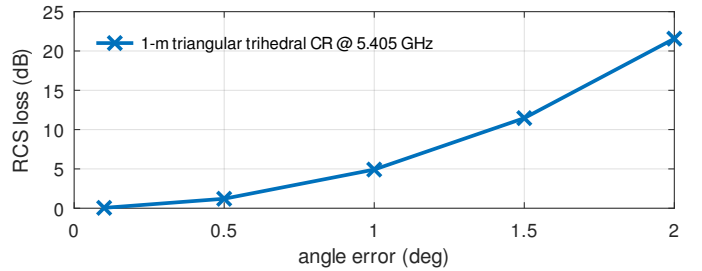
Fig. 10. Radar cross section loss as a function of orthogonality mismatch, here for a C-band corner reflector with 1-m length operating at 5.405 GHz.

From 2D-geometrical optics considerations, a beam incoming one of the sides of the corner reflector at angle ϑ_i is refracted by the dielectric layer tilted at an angle φ to the corner reflector surface to enter the dielectric at an angle ϑ' to its normal, reflected on the metallic surface and refracts again when outgoing the dielectric layer at an angle ϑ'' to its normal (Fig. 11).

The outgoing beam angle ϑ_o with respect to the corner reflector flat surface, in the same framework that defined ϑ_i, is deduced in the last equation from ϑ'', and these two refractions and reflection meet the condition (from left to right in Fig. 11)

$$\begin{cases} n \cdot \sin(\vartheta') = \sin(90° - \varphi - \vartheta_i) \\ n \cdot \sin(\vartheta' + 2\varphi) = \sin(\vartheta'') \\ \vartheta_o = 90° + \varphi - \vartheta'' \end{cases}$$

with $n = \sqrt{\varepsilon_r}$ the optical index of the dielectric layer with relative permittivity ε_r. After checking that $\vartheta_o = \vartheta_i$ when $n = 1$ (no dielectric layer) and when $\varphi = 0$ (parallel sides of the dielectric slab), we plot (Fig. 12) the difference $\vartheta_o - \vartheta_i$ for $\varepsilon_r = 1.5$ and $\varphi = 3.8°$ to match our experimental conditions in a natural environment, and $\varepsilon_r = 2.5$ for the

Fig. 11. 2D geometric analysis of the refraction of an incoming beam at angle ϑ_i into a dielectric layer with angle φ to the planar conducting layer. Greek letters in red are input parameters, in black result from geometric refraction considerations, and at the end to the right is the comparison between the ϑ_0 the output beam direction with refraction in the dielectric layer with respect to ϑ_i the outgoing reflection angle equal to the incoming angle if no dielectric layer was present. Bottom: two asymptotic cases demonstrating the validity of the analysis, when the dielectric optical index is 1 (no dielectric layer) and has no impact on the electromagnetic wave propagation ($\vartheta_o = \vartheta_i$ in absence of refracting layer) and $\varphi = 0$ (no angle between the dielectric layer and the planar conducting layer). All angles indicated in degrees.

laboratory setup. The induced deviation would be equivalent to an error to the orthogonality of the corner reflector faces and induce backscattered signal deviation to the monostatic RADAR receiver and quickly reaches the few degrees needed to justify backscattered signal losses above 10 dB.

Fig. 12. Angle between the outgoing and incoming beam in a 2D-slab of material with permittivity $\varepsilon_r = 1.5$ or 2.5 respectively, with opposite faces at an angle of $3.8°$, as a function of incoming angle.

V. DISCUSSION

The impact of a thin, low-absorption dielectric on the backscattered power has been demonstrated in a controlled setting. We have related these conclusions to environmental settings around the Ny-Ålesund/Corbel corner reflector supported with some in-situ observations of the snow and ice cover on the corner reflector. Furthermore, a temperature logger whose sensor is taped using heat-conducting tape to the corner reflector bottom surface monitors the effective surface temperature for comparison with air temperature measurements with the same sensor shielded from direct sunlight.

The experiments were concluded in May 2024 after observing that

- a corner reflector located at ground level will fill with wind blown snow and the backscattered signal vanishes until the snow is removed or melts,

- interferometric measurement of glacier ice ablation during the summer time is not realistic with the current update rate of Sentinel-1 observing the area under investigation once every 12 days. Indeed the ablation from one pass to the next should be less than half a wavelength or 2.8 cm/12 days or 2.3 mm/day. However, at the maximum of the melt season, melt rates of up to 7 cm/day are observed and rates above 1 cm/day are common during 60 consecutive days (data not shown), preventing interferometric analysis due to the phase wrapping uncertainty,

- landslide monitoring is prevented by the strong signal backscattered by the mountain slope tilted towards the incoming RADAR beam, leading to a strong background signal with the corner reflector hardly if every visible against the non-cooperative scatterers.

Despite these scenario limitation, preventing the accumulation of dielectric material in the corner reflector seems of utmost importance for the backscattered signal to remain strong under all weather conditions. While some commercial developments have introduced means of preventing snow and ice accumulation (Tre Altamira corner reflectors described at https://site.tre-altamira.com/insar-solutions/insar-corner-reflectors/ with a tight protective cover), polar regions exhibit the cooperative target to harsh conditions, and assembling a tight protective sheat appears challenging especially with square trihedral corner reflectors with sharp edges. The POL corner reflector was manufactured using planar metal sheets drilled with sub-wavelength holes hardly affecting the resulting cross section [28], and raised above wind-blown snow height, fine on a concrete slab poured over strong rock supported pillar but hardly for deployment on a glacier or landslide. Attempts to protect the corner reflector with cloth or plastic sheets all failed under strong wind and wind-blown snow was not prevented from accumulating in the corner, while greenhouse effect led to snow melting and ice forming rather than letting snow flying away. Filling the corner reflector with a homogeneous dielectric, as classically done in microwave [29] or optics (e.g. Thorlabs TIR Retroreflector Prisms), appears as a viable solution with lightweight and low permittivity material such as styrofoam.

VI. CONCLUSION

We have analyzed the impact of a thin snow (dielectric) layer on corner reflector backscattered signal, and shown how even a thin, subwavelength thick layer induces refraction and deviates the outgoing beam, preventing its reception in the monostatic RADAR setup of spaceborne remote sensing platforms. Indeed, the refraction of the incoming wave leads to effects equivalent to lack of orthogonality or non-planar sides of the corner reflector, with power backscattered at angles different from the incoming angle. The consequence is that for the use of corner reflector in polar regions, snow must be prevented from reaching the reflecting surfaces with a tight protection, or the corner reflector located high enough above ground to avoid wind-blown snow accumulation, leading to complex setups with poor mechanical stability or requiring large infrastructures such as pouring a concrete slab, hardly

compatible with the use on glacier or iceshelf surfaces. The conclusion is valid in all cases of accumulation of dielectric material, even with low microwave losses, in corner reflectors used in natural environments without periodic maintenance.

REFERENCES

[1] K. M. Larson, E. D. Gutmann, V. U. Zavorotny, J. J. Braun, M. W. Williams, and F. G. Nievinski, "Can we measure snow depth with GPS receivers?" *Geophysical research letters*, vol. 36, no. 17, 2009.

[2] L. Ferro-Famil and M. Gay, "Penetration depth of synthetic aperture radar signals in ice and snow: an analytical approach," in *Workshop Remote Sensing and Modeling of Surface Properties*, 2016.

[3] G. Luzi, E. Fernandez, F. M. Perez, and M. Crosetto, "A low cost active corner reflector to assist snow monitoring through Sentinel/1 images," in *2020 14th European Conference on Antennas and Propagation (EuCAP)*. IEEE, 2020, pp. 1–4.

[4] J. Eppler and B. T. Rabus, "The effects of dry snow on the SAR impulse response and feasibility for single channel snow water equivalent estimation," *IEEE Transactions on Geoscience and Remote Sensing*, vol. 60, pp. 1–23, 2021.

[5] J. Eppler, B. Rabus, and P. Morse, "Snow water equivalent change mapping from slope-correlated synthetic aperture radar interferometry (InSAR) phase variations," *The Cryosphere*, vol. 16, no. 4, pp. 1497–1521, 2022.

[6] H. Lievens, I. Brangers, H.-P. Marshall, T. Jonas, M. Olefs, and G. De Lannoy, "Sentinel-1 snow depth retrieval at sub-kilometer resolution over the European Alps," *The Cryosphere*, vol. 16, no. 1, pp. 159–177, 2022.

[7] J. Voglimacci-Stephanopoli, A. Wendleder, H. Lantuit, A. Langlois, S. Stettner, A. Schmitt, J.-P. Dedieu, A. Roth, and A. Royer, "Potential of X-band polarimetric synthetic aperture radar co-polar phase difference for arctic snow depth estimation," *The Cryosphere*, vol. 16, no. 6, p. 2163, 2022.

[8] A. N. Shiklomanov, "Open source science for ESO mission processing study workshop# 2: Earth information system (EIS) perspective," in *Open Source Science for ESO Mission Processing Study Workshop# 2*, 2022.

[9] I. Joughin, R. Forster, A. Gardner, B. Holt, E. Rignot, and B. Scheuchl, "Cryosphere sciences with NISAR," in *2021 IEEE International Geoscience and Remote Sensing Symposium IGARSS*. IEEE, 2021, pp. 550–553.

[10] Y.-L. S. Tsai, A. Dietz, N. Oppelt, and C. Kuenzer, "Remote sensing of snow cover using spaceborne SAR: A review," *Remote Sensing*, vol. 11, no. 12, p. 1456, 2019.

[11] C. Li, J. Yin, J. Zhao, G. Zhang, and X. Shan, "The selection of artificial corner reflectors based on RCS analysis," *Acta Geophysica*, vol. 60, pp. 43–58, 2012.

[12] A. W. Doerry, "Reflectors for SAR performance testing – second edition," 2014.

[13] U. Balss, C. Gisinger, and M. Eineder, "Measurements on the absolute 2-D and 3-D localization accuracy of TerraSAR-X," *Remote Sensing*, vol. 10, no. 4, p. 656, 2018.

[14] H. Stockman, "Communication by means of reflected power," *Proceedings of the IRE*, vol. 36, no. 10, pp. 1196–1204, 1948.

[15] H. Nagai, K. Kawashima, K. Yamashita, S. Yamaguchi, S. Sunako, R. Hasatani, Y. Sekiya, S. Nakayama, S. Ohkawa, and T. Uehara, "Sensitivity analysis of backscatter amplitude at snow-buried corner reflectors using C-/L-band SARs," in *AGU Fall Meeting Abstracts*, vol. 2020, 2020, pp. C005–0006.

[16] A. C. Polycarpou, C. A. Balanis, and P. A. Tirkas, "Radar cross section of trihedral corner reflectors: theory and experiment," *Electromagnetics*, vol. 15, no. 5, pp. 457–484, 1995.

[17] Y. Ohba, "On the radiation pattern of a corner reflector finite in width," *IEEE Transactions on Antennas and Propagation*, vol. 11, no. 2, pp. 127–132, 1963.

[18] K. Sarabandi and T.-C. Chiu, "Optimum corner reflectors for calibration of imaging radars," *IEEE Transactions on antennas and Propagation*, vol. 44, no. 10, pp. 1348–1361, 1996.

[19] D. J. Weydahl, "Analysis of ERS tandem SAR coherence from glaciers, valleys, and fjord ice on Svalbard," *IEEE Transactions on Geoscience and Remote Sensing*, vol. 39, no. 9, pp. 2029–2039, 2001.

[20] V. V. Bogorodskiĭ, C. R. Bentley, and P. Gudmandsen, *Radioglaciology*. Springer Science & Business Media, 1985, vol. 1.

[21] M. Jauvin, Y. Yan, E. Trouvé, B. Fruneau, M. Gay, and B. Girard, "Integration of corner reflectors for the monitoring of mountain glacier areas with Sentinel-1 time series," *Remote Sensing*, vol. 11, no. 8, p. 988, 2019.

[22] A. J. Bur, "Dielectric properties of polymers at microwave frequencies: a review," *Polymer*, vol. 26, no. 7, pp. 963–977, 1985.

[23] B. Givot, A. Gregory, B. Salski, F. Zentis, N. Pettit, T. Karpisz, and P. Kopyt, "A comparison of measurements of the permittivity and loss angle of polymers in the frequency range 10 GHz to 90 GHz," in *2021 15th European Conference on Antennas and Propagation (EuCAP)*. IEEE, 2021, pp. 1–5.

[24] R. Zoughi, P. J. Arias-Monje, J. Gallion, S. Sarkar, P.-H. Wang, P. Gulgunje, N. Verghese, and S. Kumar, "Microwave dielectric properties and targeted heating of polypropylene nano-composites containing carbon nanotubes and carbon black," *Polymer*, vol. 179, p. 121658, 2019.

[25] M. Garthwaite, S. Nancarrow, A. Hislop, A. Thankappan, J. Dawson, and S. Lawrie, "The design of radar corner reflectors for the Australian Geophysical Observing system," 2015.

[26] M. C. Garthwaite, "On the design of radar corner reflectors for deformation monitoring in multi-frequency InSAR," *Remote Sensing*, vol. 9, no. 7, p. 648, 2017.

[27] R. SaratPulapa, K. Srikanth, and P. Sridevi, "Corner reflectors pattern study with & without orthogonality errors," in *2015 13th International Conference on Electromagnetic Interference and Compatibility (INCEMIC)*. IEEE, 2015, pp. 196–201.

[28] A. Algafsh, M. Inggs, and A. K. Mishra, "The effect of perforating the corner reflector on maximum radar cross section," in *2016 16th Mediterranean Microwave Symposium (MMS)*. IEEE, 2016, pp. 1–4.

[29] C. Buchberger, F. Pfeiffer, and E. Biebl, "Dielectric corner reflectors for mmWave applications," *Advances in Radio Science*, vol. 17, pp. 197–203, 2019.